COMMUNICATION

Check for updates

Vacuum-deposited organic solar cells utilizing a low-bandgap non-fullerene acceptor†‡

Qihui Yue, [ID] §[ab] Songjun Liu,§[ab] Shengjie Xu,§[a] Guanhao Liu,[bc] Yuanyuan Jiang,[ab] Ying Wang [ID] [c] and Xiaozhang Zhu [ID] ⋆[ab]

In this work, a new vacuum-processable non-fullerene acceptor CBD was designed using a D–A strategy for the first time, which exhibits a low optical bandgap of 1.41 eV, and guarantees efficient light harvesting in the visible-NIR region. The optimal CBD-based vacuum-deposited organic solar cells with a planar heterojunction architecture delivered a PCE of 0.86% with a low energy loss of 0.63 eV, which indicates the great potential of D–A-type non-fullerene acceptors for vacuum-deposited solar cells.

Organic solar cells (OSCs), as a promising technology for energy conversion, have received extensive attention in recent years due to their unique advantages such as being lightweight, flexible, and their potential for large-area processing.[1–4] According to the type of materials applied in the active layers, OSCs can be divided into the two main categories of polymer-based (PSCs) and small-molecule-based (SMSCs). In contrast to polymers, small molecules exhibit the following evident merits: (1) definite molecular structures as well as molecular weights that can avoid batch-to-batch variation, which ensures the reproducibility of device performance and favours the understanding of structure–property relationships; (2) a relatively low synthetic complexity that can provide great convenience for adjustments of the molecular structure that are in direct correlation with the optoelectronic properties; (3) a strong crystallinity that is expected to bring a high mobility, which is conducive for charge

transport.[5–7] During the development of SMSCs, the key break-through was the realization of a full-vacuum-deposited SMSC (VD-SMSC) containing CuPc and PTCBI reported by Tang in 1986,[8] which then made the design of new p-type and n-type semiconductors a hot topic in the research of SMSCs. Nowadays, SMSCs have achieved remarkable power conversion efficiencies (PCEs) of over 15%, which is strongly attributed to the application of solution-processable non-fullerene electron acceptors (NFAs) developed in recent years.[9–12] Compared with their fullerene counterparts, NFAs exhibit highly-tunable absorptiono and energy levels, and high absorption extinction coefficients. Moreover, even a small driving force can drive efficient charge transfer in NFA-based devices and the carriers can transport through three-dimensional channels constructed *via* the strong π–π stacking and intermolecular interactions of NFAs.[13–15]

Besides the solution processing fabrication, vacuum deposition is also a promising technology for the commercialization of OSCs, which has been proven to be feasible during the commercialization of organic light-emitting diodes (OLEDs). Vacuum deposition technology can construct thin films relatively simply with high purity, compactness, and reproducibility, of which the thickness can be precisely controlled, even with a thickness of only a few nanometres, and meanwhile avoid organic solvent use and liquid waste treatment, which provides great convenience in the construction of OSCs, especially for multi-layer devices. Moreover, VD-SMSCs using stable and pure materials have shown excellent stability even under a high-intensity illumination.[16] However, although VD-SMSCs were developed much earlier, their performance lagged behind, with the best PCE of only 9.6% in a single-junction device[17] and 11.1% in a triple-junction device.[18] For the absorber materials, there are various p-type molecules reported in the literature,[19–23] but most of the existing high-performance VD-SMSCs are based on fullerene acceptors, such as C_{60} and C_{70}, due to their high electron affinity, excellent thermal stability, and high electron mobility. Nevertheless, the often-accompanied high energy loss (E_{loss}, defined as $E_g^{opt} - eV_{oc}$,

[a] *Beijing National Laboratory for Molecular Sciencesik, CAS Key Laboratory of Organic Solids, Institute of Chemistry, Chinese Academy of Sciences, Beijing 100190, China. E-mail: xzzhu@iccas.ac.cn*

[b] *School of Chemistry and Chemical Engineering, University of Chinese Academy of Sciences, Beijing 100049, China*

[c] *Key Laboratory of Photochemical Conversion and Optoelectronic Materials Technical Institute of Physics and Chemistry Chinese Academy of Sciences, Beijing 100190, China*

This journal is © The Royal Society of Chemistry 2022

J. Mater. Chem. C, 2022, **10**, 2569–2574 | **2569**

where E_g^{opt} is the lowest optical bandgap of the active materials and e is the elementary charge, Fig. S1a and Table S1, ESI‡), and the weak absorption of fullerenes greatly limit further improvements of performance. Rare examples based on NFAs have been reported.[24–26] For example, Cnops et al. utilized the electron donor α-6T and phthalocyanine-type NFAs (SubNc and SubPc) to construct planar heterojunction (PHJ) devices, which delivered PCEs of 6.0% and 4.7%, respectively, significantly higher than that of the fullerene-based device (PCE of 1.0%). Following the further sequential deposition of α-6T, SubNc and SubPc, the PCE was promoted to 8.4% by exploiting Förster resonance energy transfer.[24] Recently, Würthner et al. developed a series of n-type small-molecule semiconductors based on the quinoidal dicyanomethylene (DCV)-endcapped cyclopentadithiophene (CPDT), among which CPTQ-Oc realized a PCE of 0.64% in a PHJ device.[26] However insufficient spectral coverage or large E_{loss} values still exist in these systems. Therefore, taking account of the various merits of NFAs and their successful applications in solution-processed SMSCs, the design of new vacuum processable NFAs is of great importance and potential for the development of VD-SMSCs. The new materials should exhibit good sublimation properties and thermal stability, and a strong and broad absorption as well as suitable energy levels, which are indispensable properties.

The D–A strategy (D and A refer to the electron-donating and electron-accepting moieties, respectively) is a popular and effective method for designing photovoltaic materials.[13–15,27,28] By regulating D and A, respectively, the absorption and energy levels can be well controlled, which is beneficial for light harvesting and the simultaneous realization of efficient charge generation and high open-circuit voltage (V_{oc}). Herein, we applied the D–A strategy for the first time in the design of vacuum-processable NFAs, based on which, a new A–A′–D–A′–A-structured NFA named CBD with DCV as A, benzothiadiazole (BT) as A′ and CPDT as D was obtained, after which its properties were fully characterized. CBD exhibits not only a low molar weight and high thermal stability but a good light-harvesting ability and relatively high EA and IP values, which makes it a promising acceptor candidate for VD-SMSCs. To investigate the photovoltaic performance of CBD, VD-SMSCs with a PHJ structure were constructed and optimized by matching CBD with a D–A–A′-type small molecule donor. The best device demonstrated a PCE of 0.86% with a V_{oc} of 0.78 V, a short-circuit current density (J_{sc}) of 2.93 mA cm^{-2} and a fill factor (FF) of 37.58%, and the E_{loss} of this system is only 0.63 eV, which indicates that the high energy level tunability of the D–A-type NFAs is of positive significance in reducing E_{loss} (Fig. S1b and Table S2, ESI‡). These results show the great potential of D–A type NFAs in VD-SMSCs.

The synthesis route of CBD is depicted in Scheme 1. Compound 1 and 2 were reacted to offer the target molecule CBD using a Stille-coupling reaction in a yield of 61% as a dark blue solid. CBD was characterized in detail with ^{1}H-NMR, ^{13}C-NMR, and high-resolution mass spectrometry, which have been summarized in the ESI.‡ The results of the thermogravimetric analysis (TGA) under a nitrogen atmosphere (see Fig. S2, ESI‡) indicate the good thermal stability of CBD with a 5% weight loss at a temperature of 367 °C. The differential scanning
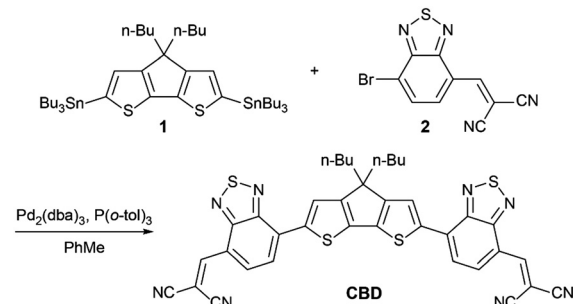
Scheme 1 Synthetic route for the small molecule CBD.

calorimetry (DSC) measurement was also performed. As shown in Fig. S3 (see the ESI‡), there are no obvious endothermic and exothermic peaks in the curve within the scan range of 50–330 °C, which indicates that the crystallinity of CBD is relatively weak. The ultraviolet-visible-near infrared (UV-vis-NIR) absorption spectra of CBD in the chloroform solution and in the solid state are shown in Fig. S4 (see the ESI‡) and Fig. 1b, and the detailed parameters are listed in Table S3 (see the ESI‡). Due to the strong intramolecular charge transfer (ICT) effect, CBD exhibits a strong and broad absorption in the visible and NIR regions. The maximum absorption peak of the solution is located at 680 nm and the molar extinction coefficient (ε_{max}) is calculated to be as high as 1.11×10^5 M^{-1} cm^{-1}. On the other hand, in the thin film, the maximum absorption peak is slightly bathochromically-shifted to 689 nm, but the absorption band is significantly broadened compared with that in the solution. The film shows a low E_g^{opt} of 1.41 eV, which may be due to the intermolecular π–π stacking. These characters are beneficial for efficient light harvesting and are very promising for application as an active layer material in organic photovoltaic devices. Cyclic voltammetry (CV) measurements were executed to probe the electrochemical properties of the CBD film (Fig. S5, ESI‡). After internal calibration of the potential using the ferrocene/ferrocenium (Fc/Fc$^+$) redox couple, it was calculated that the EA and IP are 3.84 and 5.42 eV, respectively (Fig. 1c).

To evaluate the photovoltaic performance of this new vacuum-processable material, we constructed VD-SMSCs by matching them with DTDCTB, a donor material previously reported by Wong et al. (molecular structure shown in Fig. 1a).[29] The two materials can take advantage of photons in the range of 300–880 nm, and their EA and IP values are well-matched, which provides a sufficient driving force for exciton dissociation (Fig. 1b and c). The vacuum-deposited devices adopted a PHJ structure of ITO/MoO$_x$ (5 nm)/DTDCTB/CBD/BPhen (10 nm)/Al (100 nm), where ITO is indium tin oxide, which serves as the transparent anode, and MoO$_x$ and BPhen were applied as the hole-transporting layer and electron-transporting layer, respectively (as shown in Fig. 1d). The organic materials used in the devices were all purified using temperature-gradient sublimation under vacuum conditions, after which all the layers were vacuum-deposited onto the substrate at room temperature. The photovoltaic performance
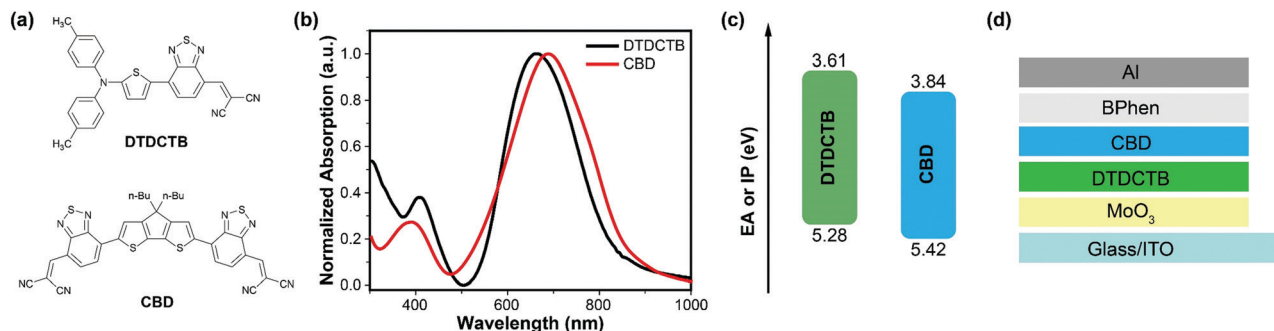
2570 | J. Mater. Chem. C, 2022, 10, 2569–2574

This journal is © The Royal Society of Chemistry 2022

Fig. 1 (a) Molecular structures of the donor DTDCTB and the acceptor **CBD**. (b) UV-vis-NIR absorption spectra. (c) EA and IP of the DTDCTB and **CBD** films and (d) device structure of the VD-SMSCs based on DTDCTB and **CBD**.

Table 1 The photovoltaic performance parameters for the PHJ VD-SMSCs based on DTDCTB and **CBD** with different active layer thicknesses under AM 1.5G illumination, 100 mW cm^{-2}

D/A thickness [nm]	V_{oc}[a] [V]	J_{sc}[a] [mA cm^{-2}]	FF[a] [%]	PCE[a] [%]
5/10	0.79	2.69	33.49	0.71
	(0.79 ± 0.01)	(2.67 ± 0.02)	(33.45 ± 0.07)	(0.70 ± 0.05)
10/20	0.78	2.93	37.58	0.86
	(0.78 ± 0.01)	(2.89 ± 0.03)	(37.24 ± 0.27)	(0.85 ± 0.02)
20/40	0.77	2.55	33.86	0.67
	(0.77 ± 0.01)	(2.53 ± 0.04)	(37.75 ± 0.15)	(0.66 ± 0.01)

[a] All the average values with standard deviations were calculated from over 10 independent devices.

was optimized by tuning the layer thicknesses of DTDCTB and **CBD** precisely. We firstly fixed the thickness of **CBD** at 20 nm, and varied the thickness of DTDCTB within the range of 5–30 nm (5, 10, 20, and 30 nm) to determine the optimal donor/acceptor thickness ratio (Fig. S6a and Table S4, ESI‡). With the thickness of DTDCTB increasing, V_{oc}, J_{sc} and FF all increased at first and then decreased, among which the former two parameters reached their maximum values at a thickness of 10 nm, while for FF this was at 20 nm, and the overall performance reached the maximum value at a donor/acceptor thickness ratio of 1 : 2. Then according to the optimal ratio, the total active layer thickness was further optimized (Table 1 and Fig. S6b, ESI‡). The best performance was achieved when the thicknesses of DTDCTB and **CBD** were 10 nm and 20 nm, respectively. Fig. 2a displays the current density–voltage (J–V) characteristics for the optimal DTDCTB/**CBD**-based VD-SMSC. Under AM 1.5G (intensity of 100 mW cm^{-2}) illumination, the best PCE is 0.86% with a V_{oc} of 0.78 V, a J_{sc} of 2.93 mA cm^{-2} and an FF of 37.58%. The E_{loss} of this optimal device is only 0.63 eV, which is attributed to the fact that the D–A strategy can adjust the energy levels flexibly, and reduce the energy offset between **CBD** and DTDCTB, thus making the energy levels of the two materials form a suitable alignment, and benefiting E_{loss} reduction. The storage stability of the optimized PHJ device without any encapsulation was also investigated as shown in Fig. S7 (see the ESI‡). During the two-week test period, the V_{oc} remained basically unchanged, J_{sc} decreased but FF increased, and the final PCE changed very little. The relevant external quantum efficiency (EQE) curve is shown in Fig. 2b. The device exhibits a broad EQE response in the wavelength region from
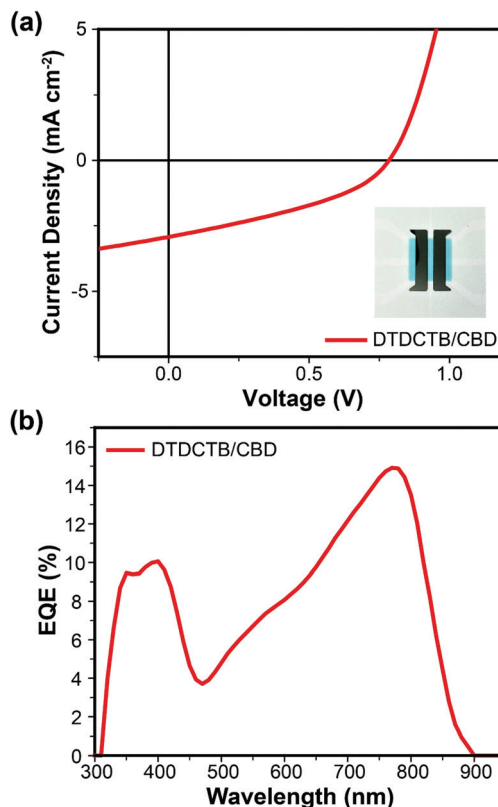

Fig. 2 (a) J–V characteristics and (b) EQE curve for the optimal VD-SMSC based on DTDCTB and **CBD** under AM 1.5G (100 mW cm^{-2}) illumination. The inset graph in (a) is a photograph of the optimal device and the effective area is 0.09 cm^2.

This journal is © The Royal Society of Chemistry 2022

J. Mater. Chem. C, 2022, **10**, 2569–2574 | **2571**

300 to 880 nm, with a maximum value of 14.9% at 770 nm, which is consistent with the absorption wavelength range of the active layer materials, and indicates that the excitons generated by **CBD** could indeed move to the interface of DTDCTB/**CBD**, and then dissociate into free charges, which further transport to the electrodes and are collected, thus contributing to the final J_{sc}. The J_{sc} offered by the integration of the EQE curve is 2.86 mA cm^{-2}, which is well-matched with the result of the J–V tests with an error within 3%, and indicates that the measurement of performance is reliable.

However, the device suffers from a relatively low J_{sc} and FF, which has a significant correlation with the probability of the exciton dissociation and charge collection ($P(E,T)$), the charge transport ability and the degree of charge recombination. The relationship between photocurrent density (J_{ph}) and effective voltage (V_{eff}) was first measured, where J_{ph} is the difference between photocurrent density under AM 1.5G illumination (J_L) and the dark current density obtained under dark conditions (J_D), and V_{eff} is defined as $V_0 - V_{app}$ (V_0 is the voltage when $J_L = J_D$ and V_{app} is the applied voltage). $P(E,T)$ is obtained by J_{ph}/J_{sat}, where J_{sat} is the saturation photocurrent density. As displayed in Fig. S8 (see the ESI‡), J_{ph} exhibits a pronounced field-dependent behaviour in the entire V_{eff} region, which indicates a relatively low $P(E,T)$, that is, the photogenerated excitons cannot be completely dissociated into free charges, which may be due to poor exciton migration or severe donor–acceptor interface recombination. Then, to study the charge recombination behaviour of the device, the dependence of V_{oc} and J_{sc} on light intensity (P_{light}) were also measured (Fig. S9, ESI‡).[30–32] The slope of V_{oc} *versus* ln P_{light} evaluates the degree of trap-assisted recombination. A slope of $2k_BT/e$ states that trap-assisted recombination is the dominant recombination mechanism in the device while the slope of k_BT/e indicates that bimolecular recombination is dominant, where k_B is the Boltzmann constant and T is the Kelvin temperature. In this **CBD**-based VD-SMSC, the slope is $1.52k_BT/e$. The relationship between J_{sc} and P_{light} can be expressed using the formula of $J_{sc} \propto P_{light}^{\alpha}$, where α is the exponential factor. If all the charges are swept out and collected without any bimolecular recombination, the value of α should be 1. The α is 0.87 in this optimal VD-SMSC. The recombination analysis demonstrates that the free charges generated by those excitons that can be dissociated successfully also encounter trap-assisted or bimolecular recombination during the charge transport process, which will cause the loss of free carriers, and affects the number of carriers that can be finally collected by the electrodes and lead to the loss of J_{sc}. Meanwhile, the FF, which is a factor that represents competition between sweep-out of the photogenerated carriers and the recombination of carriers, will also decrease. The vertical charge transport ability of the pristine **CBD** film was also investigated using the space-charge limited current (SCLC) method (Fig. S10, ESI‡), and the electron mobility (μ_e) was calculated to be 3.38×10^{-6} cm^2 V^{-1} s^{-1}. Since the charge transport ability of the film is related to the molecular stacking, grazing-incidence wide-angle X-ray scattering (GIWAXS) was applied to investigate the molecular crystallinity in the pristine **CBD** films as shown
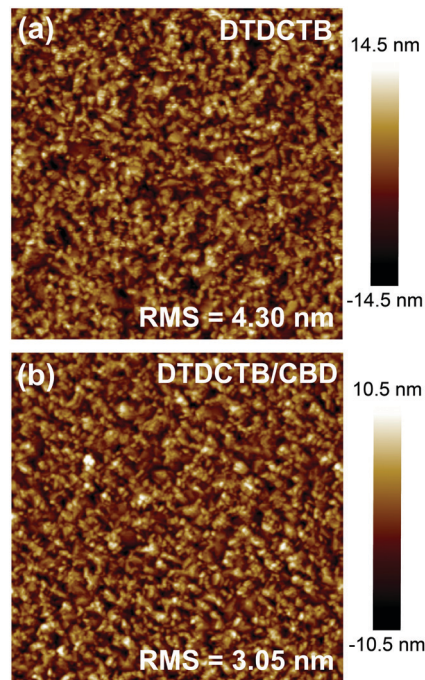

Fig. 3 Surface morphology characterization using AFM height images of (a) DTDCTB and (b) DTDCTB/**CBD** sublimated films (scan area: 3.0 μm × 3.0 μm).

in Fig. S11 (see the ESI‡). From the two-dimensional (2D) pattern, the pristine CBD film shows a broad amorphous halo, and from the corresponding 1D line-cut profiles, CBD shows wide (010) π–π stacking peaks both in the out-of-plane (OOP) and in-plane (IP) directions, which indicates that CBD adopts both face-on and edge-on orientations in the vacuum-deposited film. The crystal coherence length (CCL) values are calculated to be only 1.12 and 1.43 nm in the IP and OOP directions, which indicates weak structural order. Moreover, the charge carrier mobilities in the optimized PHJ device have also been investigated as shown in Fig. S10 (see the ESI‡). The hole mobility (μ_h) and μ_e were calculated to be 1.15×10^{-6} and 1.04×10^{-6} cm^2 V^{-1} s^{-1}, respectively. The relatively low mobilities can lead to charge recombination and greatly influence the final performance. From all the above analyses, the reasons for the relatively low J_{sc} and FF is well explained.

The surface morphology of the DTDCTB and DTDCTB/**CBD** sublimated films was characterized using the atomic force microscope (AFM) operating in tapping mode. As shown in Fig. 3a, DTDCTB forms a smooth and homogeneous layer on the substrate (ITO/MoO$_x$) without any obvious aggregates and the root-mean-square (RMS) value of this film is 4.30 nm, which indicates its moderate crystallinity. Different from the film formed by the strong crystalline material α-6T, of which the RMS value is up to 10.1 nm, which is accompanied by some spike-like peaks with a height of over 60 nm,[33,34] the smooth surface of the DTDCTB film cannot provide a sufficient contact surface for the subsequent deposited CBD film, which is also a factor limiting the performance to a certain extent. Fig. 3b shows the AFM image of the **CBD** film grown

2572 | *J. Mater. Chem. C*, 2022, **10**, 2569–2574

This journal is © The Royal Society of Chemistry 2022

on the DTDCTB film. The **CBD** film is also uniform and continuous and covers the DTDCTB layer completely, and evenly distributed larger domains are observed. The lower RMS value of 3.05 nm indicates that the film exhibits a relatively low crystallinity, which is unfavourable for charge transport, but can form a good contact with the Bphen and electrode, which benefits charge collection.

In summary, considering the prominent advantages of NFAs and their success in boosting the performance of solution processed SMSCs as well as the promising prospects of vacuum deposition technology in the commercialization of OSCs, a new A–A′–D–A′–A-structured NFA **CBD** was designed and synthesized using the D–A strategy for application in VD-SMSCs for the first time. The properties of **CBD** were fully characterized. **CBD** exhibits good thermal stability and a low molar weight but a high molar extinction coefficient, which is favourable for vacuum-deposition and light harvesting. Also, the **CBD** film shows a strong and broad absorption in the visible and NIR regions due to the strong ICT effect, which corresponds to a low E_g^{opt} of 1.41 eV, and an IP and EA of 5.42 eV and 3.84 eV, respectively. By applying DTDCTB as the donor and **CBD** as the acceptor, VD-SMSCs with a PHJ structure were constructed and the optimal device yielded a PCE of 0.86% with a V_{oc} of 0.78 V, a J_{sc} of 2.93 mA cm^{-2} and an FF of 37.58%, accompanied by a low E_{loss} of 0.63 eV. This work demonstrates the great application potential of D–A-type NFAs in VD-SMSCs. In our device, there is still room for further improvement of the J_{sc} and FF values. Further design of NFAs with higher crystallinity, for example, to enhance the molecular co-planarity, or to shorten the alkyl chain to make the molecules stack more compactly, is of great importance. Also, improvement of device processing, including device structure optimization and the adoption of substrate heating, is urged, which is beneficial for higher J_{sc} and FF values.

Conflicts of interest

There are no conflicts to declare.

Acknowledgements

References

1 G. Li, R. Zhu and Y. Yang, *Nat. Photonics*, 2012, **6**, 153–161.
2 C. Brabec, U. Scherf and V. Dyakonov, *Organic Photovoltaics: Materials, Device Physics, and Manufacturing Technologies*, Wiley-VCH Verlag GmbH & Co. KGaA, Weinheim, Germany, 2nd edn, 2014.
3 L. Lu, T. Zheng, Q. Wu, A. M. Schneider, D. Zhao and L. Yu, *Chem. Rev.*, 2015, **115**, 12666–12731.
4 O. Inganäs, *Adv. Mater.*, 2018, **30**, 1800388.
5 A. Mishra and P. Bäuerle, *Angew. Chem., Int. Ed.*, 2012, **51**, 2020–2067.
6 S. D. Collins, N. A. Ran, M. C. Heiber and T.-Q. Nguyen, *Adv. Energy Mater.*, 2017, **7**, 1602242.
7 Y. Huo, H.-L. Zhang and X. Zhan, *ACS Energy Lett.*, 2019, **4**, 1241–1250.
8 C. W. Tang, *Appl. Phys. Lett.*, 1986, **48**, 183–185.
9 N. Li, Y. Kan, K. Gao, M. Zhang, N. Li, G. Zhou, S. B. Jo, X. Shi, F. Lin, Q. Rong, F. Liu, G. Zhou and A. K.-Y. Jen, *Joule*, 2020, **4**, 2223–2226.
10 J. Ge, L. Hong, W. Song, L. Xie, J. Zhang, Z. Chen, K. Yu, R. Peng, X. Zhang and Z. Ge, *Adv. Energy Mater.*, 2021, **11**, 2100800.
11 M. Jiang, H. Bai, H. Zhi, L. Yan, H. Y. Woo, L. Tong, J. Wang, F. Zhang and Q. An, *Energy Environ. Sci.*, 2021, **14**, 3945–3953.
12 C. An, Y. Qin, T. Zhang, Q. Lv, J. Qin, S. Zhang, C. He, H. Ade and J. Hou, *J. Mater. Chem. A*, 2021, **9**, 13653–13660.
13 J. Zhang, H. Tan, X. Guo, A. Facchetti and H. Yan, *Nat. Energy*, 2018, **3**, 720–731.
14 A. Wadsworth, M. Moser, A. Marks, M. S. Little, N. Gasparini, C. J. Brabec, D. Baran and I. McCulloch, *Chem. Soc. Rev.*, 2019, **48**, 1596–1625.
15 Q. Yue, W. Liu and X. Zhu, *J. Am. Chem. Soc.*, 2020, **142**, 11613–11628.
16 Q. Burlingame, X. Huang, X. Liu, C. Jeong, C. Coburn and S. R. Forrest, *Nature*, 2019, **573**, 394–397.
17 O. L. Griffith, X. Liu, J. A. Amonoo, P. I. Djurovich, M. E. Thompson, P. F. Green and S. R. Forrest, *Phys. Rev. B: Condens. Matter Mater. Phys.*, 2015, **92**, 085404.
18 X. Che, X. Xiao, J. D. Zimmerman, D. Fan and S. R. Forrest, *Adv. Energy Mater.*, 2014, **4**, 1400568.
19 Y.-H. Chen, L.-Y. Lin, C.-W. Lu, F. Lin, Z.-Y. Huang, H.-W. Lin, P.-H. Wang, Y.-H. Liu, K.-T. Wong, J. Wen, D. J. Miller and S. B. Darling, *J. Am. Chem. Soc.*, 2012, **134**, 13616–13623.
20 V. Steinmann, N. M. Kronenberg, M. R. Lenze, S. M. Graf, D. Hertel, K. Meerholz, H. Bürckstümmer, E. V. Tulyakova and F. Würthner, *Adv. Energy Mater.*, 2011, **1**, 888–893.
21 M. Zhang, H. Wang, H. Tian, Y. Geng and C. W. Tang, *Adv. Mater.*, 2011, **23**, 4960–4964.
22 A. Mishra, D. Popovic, A. Vogt, H. Kast, T. Leitner, K. Walzer, M. Pfeiffer, E. Mena-Osteritz and P. Bäuerle, *Adv. Mater.*, 2014, **26**, 7217–7223.
23 T.-y. Li, T. Meyer, Z. Ma, J. Benduhn, C. Körner, O. Zeika, K. Vandewal and K. Leo, *J. Am. Chem. Soc.*, 2017, **139**, 13636–13639.
24 K. Cnops, B. P. Rand, D. Cheyns, B. Verreet, M. A. Empl and P. Heremans, *Nat. Commun.*, 2014, **5**, 3406.
25 I. Kim, H. M. Haverinen, Z. Wang, S. Madakuni, Y. Kim, J. Li and G. E. Jabbour, *Chem. Mater.*, 2009, **21**, 4256–4260.
26 K. Menekse, P. Chen, B. Mahlmeister, O. Anhalt, A. Kudzus, M. Stolte and F. Würthner, *J. Mater. Chem. C*, 2020, **8**, 15303–15311.

27 H. Yao, L. Ye, H. Zhang, S. Li, S. Zhang and J. Hou, *Chem. Rev.*, 2016, **116**, 7397–7457.

28 H. Tang, C. Yan, J. Huang, Z. Kan, Z. Xiao, K. Sun, G. Li and S. Lu, *Matter*, 2020, **3**, 1403–1432.

29 L.-Y. Lin, Y.-H. Chen, Z.-Y. Huang, H.-W. Lin, S.-H. Chou, F. Lin, C.-W. Chen, Y.-H. Liu and K.-T. Wong, *J. Am. Chem. Soc.*, 2011, **133**, 15822–15825.

30 M. M. Mandoc, F. B. Kooistra, J. C. Hummelen, B. de Boer and P. W. M. Blom, *Appl. Phys. Lett.*, 2007, **91**, 263505.

31 S. R. Cowan, A. Roy and A. J. Heeger, *Phys. Rev. B: Condens. Matter Mater. Phys.*, 2010, **82**, 245207.

32 S. R. Cowan, J. Wang, J. Yi, Y.-J. Lee, D. C. Olson and J. W. P. Hsu, *J. Appl. Phys.*, 2013, **113**, 154504.

33 J. Sakai, T. Taima and K. Saito, *Org. Electron.*, 2008, **9**, 582–590.

34 V. C. Nikolis, J. Benduhn, F. Holzmueller, F. Piersimoni, M. Lau, O. Zeika, D. Neher, C. Koerner, D. Spoltore and K. Vandewal, *Adv. Energy Mater.*, 2017, **7**, 1700855.